Journal of
Materials Chemistry A

Materials for energy and sustainability

Accepted Manuscript

ROYAL SOCIETY OF CHEMISTRY

rsc.li/materials-a

View Article Online
DOI: 10.1039/C9TA04165F

ARTICLE

Direct Synthesis of Electrowettable Nanostructured Hybrid Diamond

Received 00th January 20xx,
Accepted 00th January 20xx

DOI: 10.1039/x0xx00000x

Sujit Deshmukh[a,b], Kamatchi Jothiramalingam Sankaran[c,d], Debosmita Banerjee[a], Chien-Jui Yeh[e], Key-Chyang Leou[e], Deodatta Maheshwar Phase[f], Mukul Gupta[f], I-Nan Lin[g], Ken Haenen[c,d], Susanta Sinha Roy[a*], Prashant. R. Waghmare[b*]

The possibilities of precise control over wetting characteristics of carbon based hybrid nanostructures consisting of both sp^2 and sp^3 hybridized carbon, using electrowetting technique are demonstrated. A fascinating polarity dependent electrowetting behavior in the presence of an electrolyte, follows an abrupt transition from highly hydrophobic (contact angle ~ 142°) Cassie-Baxter states to a hydrophilic (~ 30°) Wenzel state where diamond films are acting as anode. In addition, we also report a remarkable transition from weakly hydrophobic to nearly superhydrophobic diamond nanostructures by chemical and morphological manipulation. The unique structural properties with precisely tailored morphology and surface roughness enable such transitions on the nanostructured surface. This approach of preparing environmental stable hydrophobic surfaces with polarity dependent wetting and precise control of the wetting mode transition, could be used to numerous applications, such as, electrochemical transport of liquid, supercapacitors, low friction microfluidics etc.

Introduction

Nanostructured surfaces with controllable wetting characteristics have been subjected to great attention in various applications such as, microfluidics, biosensing and biofunctionalization, painting, and drug delivery.[1-6] Particularly, some applications involve the interaction between different polarity, ionic or protic liquids with the engineered lower energy surfaces.[7] Smooth, homogeneous and solid surfaces have inherent surface energy which require a specialized treatment to be considered as low energy surfaces. Either the change in surface roughness[8] or chemical heterogeneity at the surface or in some cases, both are the key requirements for obtaining low energy surfaces on which one can observe the omniphobicity.[9-13] Therefore, worldwide numerous techniques have been successfully adopted to obtain such surfaces depicting liquid repellency.[14] The challenging task is to tune the wettability on demand which can be achieved with the electrowetting either in reversible or irreversible way.[15] An external actuation in terms of potential difference can permit the variation in wettability from superhydrophobic to superhydrophilic.[16] It is interesting to develop a material with a single step approach that is not only accessible for surface or chemical heterogeneity but also eligible to be a substrate for electrowetting or electrospreading.

Since the last decade, synthesis of nanocarbons with their one-dimensional, two-dimensional, and three-dimensional structural arrangement has drawn a large wave of excitement in the research community for their wide ranges of applications.[17-20] Diamond is one of the key member of this carbon family and due to its unique physical and chemical properties, it has shown promising applicability in numerous technological fields such as, energy storage,[21] electrochemical sensors,[22, 23] and field electron emitter devices.[24] In recent years, control over the wetting characteristics of nanocrystalline diamond (NCD) and preparing a diamond surface which can be tuned easily for variable wettability has gained considerable interest in biomedical arena ever since this material was proposed to be perfectly biocompatible.[25-28] A common approach of changing the wettability by means of changing the chemical signature of the interface or the surface roughness has been adopted, for example, hydrogen terminated diamond,[29] oxidized diamond,[30] doped with external element,[31] ion implanted diamond[32], plasma etched,[33] functionalized[34], etc. However, chemical modifications have some drawbacks in long term functioning, i.e., durability and surface heterogeneity approach is complex in nature to engineer.[35] Alternatively, Pu *et al.*[18] have shown the wetting of graphene/carbon nanotube composites by external electric fields, mimicking the electrowetting scenario. Similarly, the wettability of bucky papers has changed from superhydrophobic to superhydrophilic by means of electrowetting.[36] It is known that the great versatility of carbon materials mainly comes from the strong

[a] Department of Physics, School of Natural Sciences, Shiv Nadar University, NH-91, Uttar Pradesh 201314, India.
[b] interfacial Science and Surface Engineering Lab (iSSELab), Department of Mechanical Engineering, University of Alberta, Edmonton, Alberta T6G2G8, Canada
[c] Institute for Materials Research (IMO), Hasselt University, Diepenbeek, Belgium.
[d] IMOMEC, IMEC vzw, Diepenbeek, Belgium.
[e] Department of Engineering and System Science, National Tsing Hua University, Hsinchu, Taiwan, Republic of China.
[f] UGC-DAE Consortium for Scientific Research, University Campus, Khandwa Road, Indore 452017, India.
[g] Department of Physics, Tamkang University, Tamsui, Taiwan, Republic of China.
† Footnotes relating to the title and/or authors should appear here.
Electronic Supplementary Information (ESI) available: [details of any supplementary information available should be included here]. See DOI: 10.1039/x0xx00000x

dependency of their structural and electrical properties on the proportion of sp^2 to sp^3 hybridized carbon atoms.[37, 38] Up to now attempts have been made to integrate two sp^2 bonded carbon materials in order to get electrowettable surfaces,[18, 39, 40] but interestingly, liquid repellency and electrospreading behavior by influencing the ratio of sp^2 to sp^3 in carbon nanostructure are still unexplored.

The development of sp^2 on sp^3 (diamond) carbon technology is believed to be very promising from the technological viewpoint. Especially the growth of sp^2 carbon on diamond in a single step process can provide a major breakthrough in the field of electrochemical sensors, fuel cells, energy storage devices, etc., where wettability control is a prime factor for better device performances.[41, 42] Substantial efforts have been made to fabricate low surface energy conducting hydrophobic films, but complex instrumentation makes the synthesis very sophisticated.[18, 43-46] Here, a feasible and economically viable method is presented to obtain nearly superhydrophobic surfaces which show promising response to external actuation demonstrating the electrospreading capability.

Therefore, in the present work, the combined effect of both sp^2 and sp^3 bonded carbons on their hydrophobicity and electrowettability has been tested by preparing a series of hydrophobic NCD films using microwave plasma enhanced chemical vapor deposition (MWPECVD) reactor where mere variation of carbon source (CH_4) concentration (1-15 %) in $CH_4/N_2/H_2$ gas mixtures resulted in significantly different NCD surfaces. Moreover, a route for the production of nearly superhydrophobic needle-like highly conductive core-shell diamond structures grown at high CH_4 concentration (15%) is also described. The factors leading to the morphological and microstructural changes have been investigated using scanning electron microscopy (SEM), X-ray diffraction (XRD), Raman spectroscopy, X-ray absorption near edge spectroscopy (XANES), and high resolution transmission electron microscopy (HR-TEM). Quantified remarks on the influence of surface chemical groups, microstructure, morphology, and roughness on the surface hydrophobicity and electrowetting properties of the NCD films will open pathways for producing a new class of conducting, environmental stable, and electrowettable hydrophobic carbon materials.

Experimental

The NCD films were grown on *n*-type Si (100) (1-20 Ω.cm, 1×1 cm^2) substrates using an MWPECVD (ASTeX 6500 series) reactor. Before the growth of the NCD films, the Si substrates were nucleated with a colloidal suspension containing ultradispersed detonation nanodiamond (size of 6-7 nm) and distilled water using spin coating method. The details of this process can be found elsewhere.[47] The NCD films were grown in the gas mixtures of CH_4, H_2 and N_2 with a microwave power of 3000 W and a pressure of 65 Torr. The CH_4 was varied from 1% (3 sccm) to 15% (45 sccm) and complemented by H_2, whereas the N_2 was kept constant at 3% (9 sccm) to maintain a total flow rate of 300 sccm (standard cubic centimetre). The grown samples were designated as "NCD_Z" films, where Z is the percentage CH_4 concentration (CC) in the gas phase varying from 1 to 15%.

The surface morphology of the NCD films was characterized using a FEI Quanta 200 FEG scanning electron microscope (SEM) operated at 15 kV. XRD was performed using Bruker, D8-discover with Cu-K_α energy (λ = 0.154 nm). The surface topography images were recorded using atomic force microscopy (AFM, XE7, Park system) in non-contact mode. The local bonding environment of the NCD films was investigated using X-ray absorption near edge spectroscopy (XANES), where XANES measurements were performed at room temperature in total electron yield mode at the polarized light soft x-ray absorption beamline (BL-1) of the Indus-2 synchrotron radiation source at Raja Raman Centre for Advance Technology, Indore, India. The Raman spectra were recorded using a Renishaw Raman spectrometer (inVia) using a 532 nm laser source, using nominal power of 25 mW for 60 s, 50× magnification. The microstructure and bonding structure of the samples were investigated using transmission electron microscopy (TEM, Joel 2100F). The preparation of TEM samples involves the following steps: first, the NCD samples were cut into appropriate size and cleaned with acetone. Then the samples were placed upside down on a glass substrate using epoxy, projecting silicon on top. The silicon was removed using sand paper grinding method. Then a copper grid was adhered on to the selected sample area and detached the copper grid with the selected sample from the glass substrate using acetone. The samples were further thin down using Argon ion-milling technique (PIPS). A software controlled needle dosing system (DSA 100E, KRÜSS GmbH) was used for electrowetting and contact angle measurement purpose. Electrolyte (1M KCl) drops of 4 µl volume and a dc bias in the range of -30 to +30V were applied for electrowetting experiment.

Results and discussion

A schematic of the electrowetting setup is shown in Figure 1a and the variations in the contact angle (CA) for a given potential difference ranging from -30 V to 30 V for all five NCDz are presented in Figure 1b. The snapshots provided in Figure 1c-e depict the droplet profiles at particular potential of -30 V, 0 V and 30 V for NCD_1, NCD_5, and NCD_{15} respectively. A gradual decrease of CA of NCD_1 and NCD_3 films with increasing external potential (both +ve and –ve cycles) can be seen from Figure 1b. These results are quite different from the previously reported results on smooth surfaces where a rapid CA saturation is observed.[15] Interestingly, in case of the NCD_5 sample, the droplet behavior switched rapidly in a nonreversible fashion from hydrophobic Cassie-Baxter state (CA~130°) to hydrophilic Wenzel (CA~75°) state with a small dc bias of 5 V. Upon further increasing the potential, CA decreased at a slower rate and it almost saturated (around 30°) after 20 V. However, the transition from hydrophobic to hydrophilic state required a higher voltage in case of NCD_{10} (CA changing from 136 ° to 70° with applied potential 15 V) and NCD_{15} sample (CA changing from 142° to 54° with applied potential 15 V) as compared to the NCD_5 sample. Another interesting observation to note that, for the NCD hybrids prepared at higher CC (5% and 10%), especially in NCD_5 sample, the droplet spreading is also depending on the applied voltage polarity on the NCD film electrodes. For a maximum negative applied potential of 30 V the minimum CA was achieved on NCD_3 and NCD_{15} (~ 45°) whereas in case of the NCD_5 the value is highest (~ 105°). For positive 30 V, the minimum CA was for NCD_5 (~ 28°) and maximum was observed with NCD_1 (~ 65°). These results suggest that NCD_5 can be a common substrate for extreme behaviors. Careful observation of each five samples shows that three

View Article Online
DOI: 10.1039/C9TA04165F

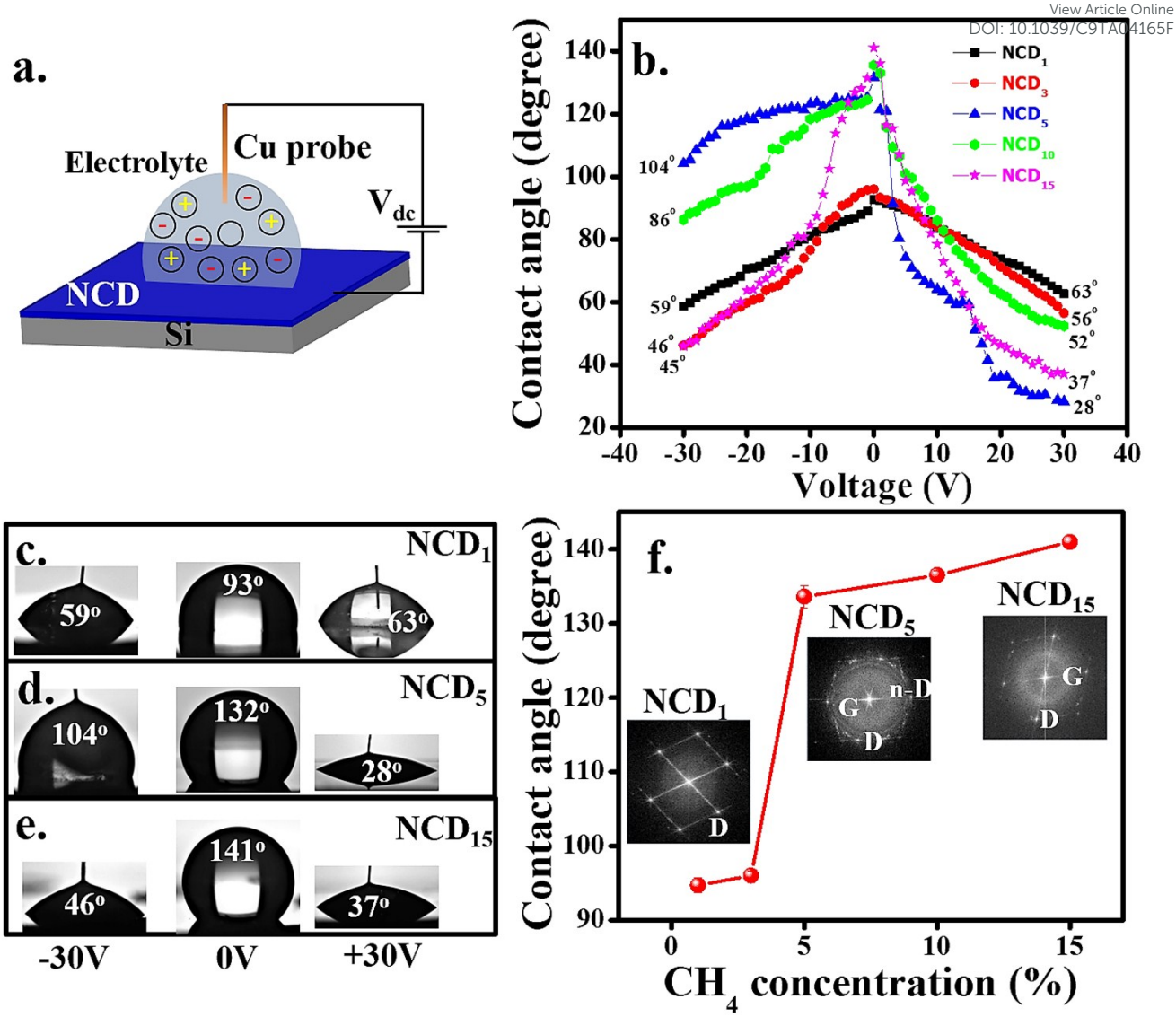

Figure 1(a) Schematic of electrowetting set up. (b) Electrowetting behavior of NCD films. Panels (c-e) display the droplet images of 1M KCl at +30V, no bias and -30V applied bias on the NCD_1, NCD_5, and NCD_{15} surfaces. (f) Plot of water contact angle as a function of CH_4 concentration. The insets showing the SAED patterns corresponding to HR-TEM images of NCD_1, NCD_5 and NCD_{15} films.

different transitions can be witnessed, namely Cassie Baxter (CB) to Wenzel (Wn), CB to CB+Wn, and Wn to Wn. The details are summarized in Table 1. The fascinating polarity dependent electrospreading behavior of NCD films with external applied potential, could be very significant for many applications.[42, 48]

Surface wettability is also fundamentally important to understand the surface energy (SE) and surface adhesion properties, which are usually characterized by measuring water contact angle (WCA) values. Figure 1f shows the plot of WCA as a function of increasing CC. The insets represent the Fourier transformed (FT) diffractogram images corresponding to the whole high resolution TEM (HR-TEM) micrographs of NCD_1, NCD_5 and NCD_{15} films (discussed in detail later), where D, G and n-D represent diamond, graphite and n-diamond (a metastable diamond) phases, respectively. It can be seen from the plot that the NCD films prepared with low CC (1% and 3%) where the diamond phase dominates the NCD surface, are weakly hydrophobic (θ_{NCD1} = 94°, θ_{NCD3} = 95°) whereas NCD_5 and NCD_{10} show WCA values around 133°. It is interesting to observe that the hybrid carbon nanostructures (both diamond and graphite phases are present) prepared using 15% CC display nearly superhydrophobic behavior ($\theta_{NCD15} \sim 142°$).

There are many factors, such as surface morphology, roughness, relative proportion of sp^2 or sp^3 bonds, presence of dangling bonds, etc. which can influence the surface energy, and in turn the wettability of the NCD films.[11, 49] The irreversible electrospreading of the aqueous electrolytes is another aspect that requires further analysis in terms of identifying the changes in the chemical composition along with the physical changes. In order to explain the genuine factors responsible for the observed changes in wettability and corresponding electrospreading behavior, spectroscopic and microscopic tools are employed to investigate the morphology, surface roughness, local bonding states and microstructural evolution of NCD films with increasing CH_4 concentration in detail.

The morphological evolution of NCD films with increasing CC is shown in Figure 2a-e. A clear picture of well faceted diamond grains (grain size ~550 nm) with distinguishable edges can be seen for NCD_1 (Figure 2a). Contrary to the faceted geometry for NCD_1, with increasing CC (3%, 5% and 10%), the sharp edged micron sized crystals are replaced by roundish granular grains with a grain size values are reduced to 20 nm for NCD_{10} (Figure 2d). Opposing to the decrease in grain size, a dramatic change in surface morphology with randomly oriented needle-like geometry (~50-80 nm in diameter and ~200-300 nm in length) is observed for the sample prepared at 15% CC (Figure 2e). Besides the change in surface morphology, the thickness of the films also increases with the increase in CC (Figure S1, supporting information).

To quantify the surface roughness of the NCD films, AFM measurements were also carried out in non-contact mode. The roughness of polycrystalline diamond depends on several aspects such as, growth chemistry, thickness, grain orientation.[50, 51] The AFM topography images are shown in the insets of Figure 2(a-e) and the variation in surface roughness with increasing CC is plotted in Figure 2f. The surface roughness value increases monotonously from 22.76 to 51.16 nm with the increase of CC from 1-15% in the growth plasma. It is also noticeable that the surface roughness of the diamond films coarsens as the film thickness increases. These results are well supported by the findings of Montaño-Figueroa *et al.*[12] The morphological parameters such as film thickness and surface roughness values are listed in Table 1. The change in surface roughness has a direct impact on the wettability and electrowetting properties of the NCD films, which is discussed in detail later.

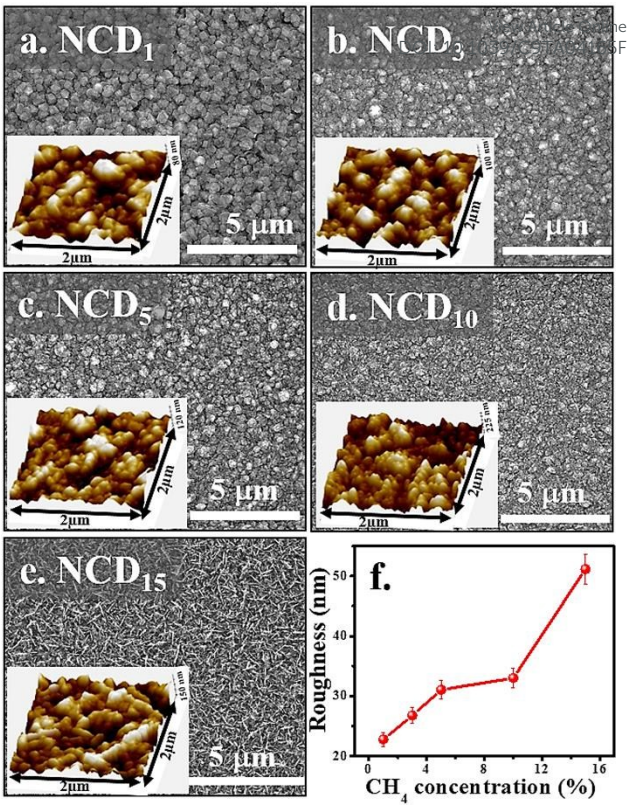

Figure 2 SEM micrographs of NCD films grown by (a) 1% (b) 3% (c) 5% (d) 10% and (e) 15% CH_4 concentration in growth plasma during CVD deposition. The insets represents their AFM topography images in non-contact mode. (f) Plot of surface roughness as a function of CH_4 concentration.

Table 1 Electrowetting results and morphological parameters of NCD films.
CA_0: Contact angle without bias; CA_{+30}: Contact angle after +30 V bias (wetting transition); ΔCA_{+30}: change in contact angle after +30 V bias; CA_{-30}: Contact angle after -30 V bias (wetting transition); ΔCA_{-30}: change in contact angle after -30 V bias; γ: film roughness; t: films thickness.

Sample code	CA_0	CA_{+30}	ΔCA_{+30}	CA_{-30}	ΔCA_{-30}	γ (µm)	t (nm)
NCD_1	93	63 (Wn → Wn)	30	59 (Wn → Wn)	34	0.62	22.76
NCD_3	95	56 (Wn → Wn)	39	46 (Wn → Wn)	49	1.12	26.74
NCD_5	133	28 (CB → Wn)	105	104 (CB → CB +Wn)	29	1.43	31.04
NCD_{10}	135	52 (CB → Wn)	83	86 (CB → CB +Wn)	49	1.87	33.02
NCD_{15}	142	37 (CB → Wn)	105	45 (CB → Wn)	97	2.06	51.16

XRD measurements were carried out for the NCDz samples and the results are shown in Figure 3a. Two peaks are observed at 2θ = 44° and 75.5° for all the samples (irrespective of their intensity differences) corresponding to the (111) and (220) reflections of polycrystalline diamond. At low CC (1% and 3%) the XRD lines are in close proximity of diamond phase purity. With increasing CC (5% and 10%) the intensity of the (111) line decreases, whereas the intensity of the (220) reflection almost remains same. This result indicates first of all the deterioration of the diamond crystal symmetry and secondly, the diamond grains are randomly oriented at low CC, while (220) planes tend to be more parallel to the substrate surface with increasing CC. Moreover, the full width at half maximum (FWHM) of the (111) peaks increases with increasing CC i.e. the grain size decreases with increasing CC which is consistent with the SEM observations (cf. Figure 2). Interestingly, for the NCD_{15} sample (spectrum (v) in Figure 3a), a new feature is observed at 2θ = 26°,

View Article Online
DOI: 10.1039/C9TA04155F

corresponding to the (002) planes of disordered graphite. The interplanar distance (d_{002}) is 0.34 nm which is similar for graphitized carbons[52, 53] These results evidence a systematic transformation in crystal structure from pure diamond to a diamond/graphite composite with the increase of CH_4 concentration. XRD pattern of Si (100) substrate is also presented in the Figure S2(a) (supporting information) which consists of single diffraction peak associated with Si (400) at 2θ=69.05°.[72] It is to be noted that the Si (400) peak is completely absent in the XRD patterns of NCD films which confirms that there is no effect of Si(100) substrate in the XRD results of NCDz.

In order to discriminate different carbonaceous phases (graphitic, amorphous, diamond like carbon) present in the NCD films, Raman measurements were also carried out. The spectrum (i) in Figure 3b exhibits only the first order sharp Raman feature of diamond centered around 1334 cm^{-1}, suggesting a high quality diamond film is grown at low CC (1%). When CC rises to 3% the diamond line disappears with the addition of new large bands centered around 1140, 1360, 1470, 1552 cm^{-1} (spectrum (ii) in Figure 3b). This large feature in the middle of 1350 and 1550 cm^{-1} is characteristic of amorphous or diamond like carbons. In the literature they are described as the short range π bonded clusters surrounded by the sp^3 bonded carbon.[54] The characteristic Raman features of disordered graphite centered around 1580 (G peak) and 1350 cm^{-1} (D peak) are observed for the samples prepared with CC higher than 3% (spectra (iii-v) in Figure 3b). In addition, a broad second order 2D peak around 2710 cm^{-1} and a combination of D and G peaks around 2940 cm^{-1} can also be seen for NCD_5, NCD_{10} and NCD_{15} sample. The peak ~ 2940 cm^{-1} signifies that the two 1st order modes (D and G) originate from the same regions of sp^2 bonded microcrystalline graphite, i.e. the film structure is dominated by sp^2 bonded carbon.[55] Though regions of sp^3 bonded carbon can be present in the films, they are not detected in Raman measurements as the magnitude of the Raman scattering tensor of graphite is 30 times more than that of diamond.[56] Therefore, high quality diamond with faceted geometry is mainly associated with low CC and the quality of the diamond in the thin film gradually degrades with increasing CC. This is explained by the creation of aromatic hydrocarbon in gas phase deposition, which condenses on the growing diamond surface and helping the formation of amorphous carbon (a-C).[57,58]Raman analyses, therefore, provide a clear picture of transformation from pure diamond to microcrystalline graphite dominated diamond with increasing CH_4 concentration, which are in good agreement with the XRD results (cf. Figure 3a). Raman spectrum of Si (100) is also displayed in the Figure S2(b) (supporting information). The recorded Raman spectrum contains a sharp peak around 520 cm^{-1} with an addition broad hump around 970 cm^{-1}. These two peaks are the characteristics of crystalline silicon.[73] The absence of these peaks in the Raman spectra of NCDz films confirms that the Si (100) substrate has no influence on the Raman spectra of NCDz.

To probe the short range bonding environment of carbon atoms and to quantify the sp^2 content in the diamond samples we further carried out XANES measurements at carbon K-edge. For comparison we have also included XANES spectrum of standard graphite. The XANES spectra of NCD films exhibit mainly three peaks centered around 285 eV, 287 eV, and a sharp absorption edge near 289 eV.

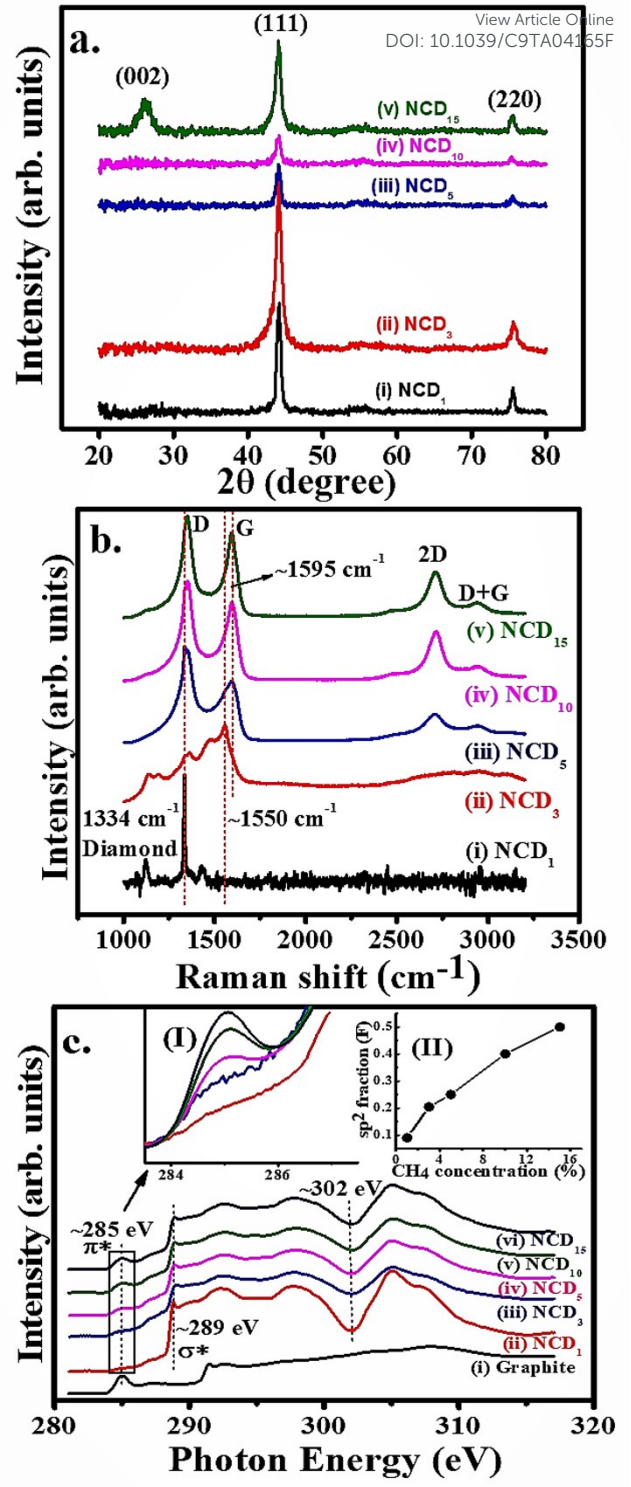

Figure 3 (a) and (b) X-ray diffraction pattern and Raman spectra of (i) NCD_1 (ii) NCD_3 (iii) NCD_5 (iv) NCD_{10} and (v) NCD_{15}. (c) Normalized C-K edge XANES spectra of (i) graphite (ii) NCD_1 (iii) NCD_3 (iv) NCD_5 (v) NCD_{10} and (vi) NCD_{15}. Standard XANES spectrum of graphite is shown for comparison. The insets of 2(c) displays (I) magnified π* region around 285 eV for all the samples. (II) Fraction of sp^2 bonded atoms vs. CH_4 concentration plot.

The broad band threshold at 289 eV is related to the 1s → σ* transition of sp^3 bonded carbon and the density of states above this

View Article Online
DOI: 10.1039/C9TA04165F

peak is controlled by the more pronounced second band gap dip of diamond around 302 eV. The peak ~285 eV is assigned to the 1s → π* transition of sp^2 bonded carbon,[59] whereas the small shoulder peak ~287 eV is associated with the chemisorbed oxygen functionalities (C=O).[60] In addition, the XANES spectrum of graphite displays an absorption edge near 291.4 eV (1s → σ* of sp^2 bonded carbon). Looking at the XANES, starting from the low CC (spectrum (ii) of Figure 3c), we can see a prominent exciton peak at 289 eV and distinct second band gap dip of diamond ~302 eV, indicating a pure diamond structure. At the level of 3% CC (spectrum (iii) of Figure 3c) the strength of the σ* feature is reduced and the sp^2 π* peak starts to appear, indicating the appearance of defect states within the band gap.[61] At higher CC (>3%), the diamond films contain many more defects and we found the strength of the π* feature at 285 eV is maximum for the NCD_{15} sample (inset (I) of Figure 3c). To quantify the fraction of sp^2 bonded atoms, we have integrated the intensity over a small energy window (283-287 eV).[62] The resulting sp^2 fraction (denoted as F) is plotted as a function of CC in the inset (II) of Figure 3c. The NCD_1 sample shows the smallest value of F, corresponding to the highest fraction of sp^3 bonded carbon, as confirmed from Raman studies as well (cf. Figure 3b). Therefore, it is clear that, with increasing CC the NCD films undergo a transformation from pure diamond to disordered graphite embedded diamond structure, and a strong agreement does exist between XRD, Raman, and XANES measurements.

To get an insight of the local bonding environment of oxygen atoms, oxygen-K (O-K) edge XANES spectra of NCD_1, NCD_5 and NCD_{15} are further investigated. The recorded O-K edge spectra (Figure S3, supporting information) display two peaks A (~533 eV) and B (~536 eV) in π* region corresponds to C-O (epoxides) and C=O (carboxylic groups) respectively.[74, 75] The overlapped O-K edge spectra clearly displays that NCD_5 has the highest percentage of oxygen containing functional groups at the π* region.

The microstructure of these NCD films were examined using TEM in order to investigate in detail the wetting characteristics of these films. Figure $4a_1$ illustrates the typical well-faceted grains of the sample NCD_1, in which only the grains oriented near some zone-axis strongly diffract electrons and show high contrast. The adjacent grains are oriented away from any zone-axis, showing low contrast. The diffraction spots in the selected area electron diffraction (SAED) pattern (inset of Figure $4a_1$) are discrete rather than continuous diffraction rings, indicating that larger and randomly oriented grains are contributing to the diffraction spots. In addition, very sharp grain boundaries with negligible thickness are observed in these films. The microstructure of this material is best illustrated by the composed dark field (c-DF) TEM images, in which the TEM dark field images are taken from the different diffraction spots of the SAED (designated in the inset of Figure $4a_2$) and were then superimposed. Furthermore, the detailed microstructure of region "A" in NCD_1 films is clarified by the HR-TEM micrograph in Figure 5a, which reveals that the diamond grains contain a complicated microstructure. The FT diffractogram of the whole structure image (FT_{0a}) designates that the diamond film is mainly of cubic diamond structure (3C diamond) oriented via the [011] zone axis. The ft_{a1} and ft_{a2} images of the designated regions "a1" and "a2" represent the presence of planar defects, seemingly stacking faults, which is entailed by the presence of rel-rod associated with each major diffraction spots in ft_{a1} and ft_{a2} images.

Increasing the CH_4 concentration to 5% markedly alters the microstructure of the NCD films. Figure $4b_1$ displays the bright field TEM (BF-TEM) microstructure of the sample NCD_5, which shows that, besides the existence of large diamond grains of size ~ 100-200 nm in these films, there is also a presence of small diamond clusters of

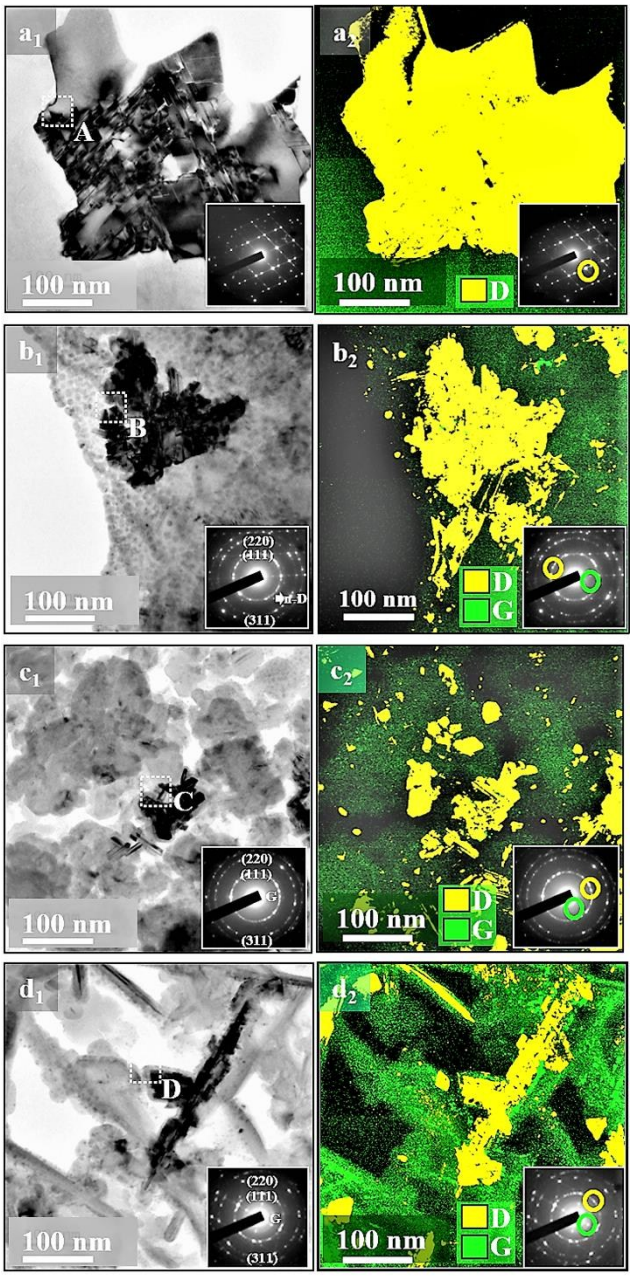

Figure 4 (a_1, b_1, c_1, and d_1) Bright field TEM micrographs of NCD films grown using 1%, 5%, 10% and 15% CH_4 concentration with inset shows their corresponding SAED pattern and (a_2, b_2, c_2, and d_2) dark field TEM images of regions "A", "B" ,"C" , and "D" in "a_1", "b_1", "c_1", and "d_1".

size < 20 nm. A clearer illustration of such a microstructure is in the c-DF-TEM micrograph shown in Figure $4b_2$. The yellow colored feature corresponds to the yellow spot in the (111) ring of the SAED pattern (inset, Figure $4b_2$), signifying the co-existence of large and

View Article Online
DOI: 10.1039/C9TA04165F

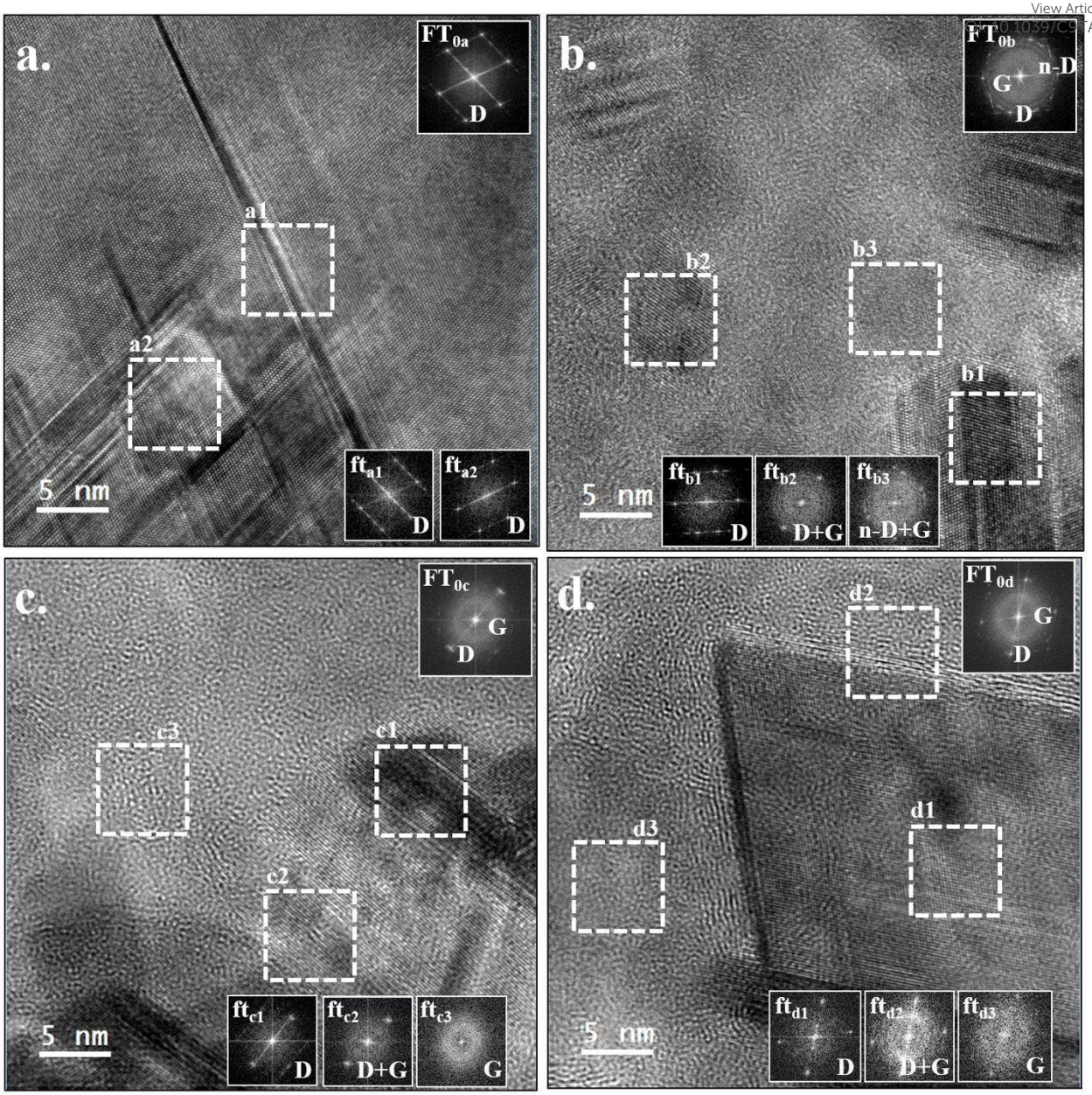

Figure 5 (a) HR-TEM image of NCD films grown using 1% CH_4 concentration corresponding to the region "A" in Figure 4a_1. The inset (FT_{0a}) displays the Fourier-transformed (FT) image corresponding to the whole structure image in "a", whereas the ft_{a1} and ft_{a2} images show the FT images corresponding to regions "a1 and a2". (b) HR-TEM image of NCD films grown using 5% CH_4 concentration corresponding to the region "B" in Figure 4b_1. The inset (FT_{0b}) displays the Fourier-transformed (FT) image corresponding to the whole structure image in "b", whereas the ft_{b1}, ft_{b2} and ft_{b3} images show the FT images corresponding to regions "b1", "b2" and b3". (c) HR-TEM image of NCD films grown using 10% CH_4 concentration corresponding to the region "C" in Figure 4c_1. The inset (FT_{0c}) displays the Fourier-transformed (FT) image corresponding to the whole structure image in "c", whereas the ft_{c1}, ft_{c2} and ft_{c3} images show the FT images corresponding to regions "c1", "c2" and c3". (d) HR-TEM image of NCD films grown using 15% CH_4 concentration corresponding to the region "D" in Figure 4d_1. The inset (FT_{0d}) displays the Fourier-transformed (FT) image corresponding to the whole structure image in "d", whereas the ft_{d1}, ft_{d2} and ft_{d3} images show the FT images corresponding to regions "d1", "d2" and d3".

nano-sized diamond grains. On the contrary, the green colored feature in line with the green spot in the SAED pattern (inset, Figure 4b_2) reveals the presence of graphitic phases in the NCD_5 films. Surprisingly, the extra diffraction spots which are arranged in a ring correspond to (200) of *n-D*; pointed out by arrow in the inset of Figure 4b_1. The *n-D* is an allotropic form of diamond with a space group of Fm3m symmetry and a cell parameter of 0.356 nm.[63, 64] Furthermore, the identification of different phase constituents in NCD_5 films is investigated in detail by HR-TEM studies. Figure 5b shows the TEM structure image which is corresponding to the region "B" in Figure 4b_1. A spotted diffraction pattern arranged in a ring in the FT diffractogram of the whole structure image (FT_{0b}) represents the randomly oriented diamond (D) grains, a diffused diffraction ring located at the canter corresponds to sp^2-bonded carbon (*a-C* or

graphitic phase) and the diffracted spots located outside the (111) diamond diffraction spots show the presence of *n-D* clusters. The FT images, ft_{b1}, ft_{b2}, and ft_{b3}, are corresponding to the regions "b1", "b2" and "b3" in Figure 5b, emphasize the diamond (D), graphite (G) and *n-D* phases, respectively.

Further increase in the CH_4 concentration to 10%, the BF-TEM image of the sample NCD_{10} films (Figure $4c_1$) illustrates that the clusters in the film contain uniformly size distributed (~ tens of nanometers) randomly oriented spherical particulates. A clear boundary exists between each spherical particulate. The SAED pattern in the inset of Figure $4c_1$ discloses strong diffraction rings which are corresponding to (111), (220) and (311) lattice planes of diamond materials, validating that these materials are diamond. No extra diffraction ring besides the diamond rings is detected in this SAED pattern of NCD_{10} films, which indicates that the formation of a metastable form of diamond clusters is efficiently concealed because of the addition of more CH_4 in the growing plasma for NCD_{10} films. The c-DF TEM images (Figure $4c_2$) taken from two diffraction spots (the inset of Figure $4c_2$) disclose that the clusters of diamond phase (yellow color) are interspersed by sp^2 bonded graphitic phases (green color). The HR-TEM image corresponding to region "C" in Figure $4c_1$ is shown in Figure 5c. The FT diffractogram of the whole structure image (FT_{0c}) shows the spotted diffraction pattern arranged in a ring is of diamond (D) phase and a diffused ring located at the center matches up to sp^2-bonded carbon. The presence of diamond (region "c1"), the co-existence of diamond and graphite (region "c2"), and graphite phases (region "c3") are highlighted by ft-images, ft_{c1}, ft_{c1}, and ft_{c3}, respectively.

It is exciting to examine the sample NCD_{15} that the granular structure of the diamond changes significantly. The diamond grains evolved into needle-like geometry from equal-axed geometry. The BF-TEM micrograph of the sample NCD_{15} films depicts in Figure $4d_1$ clearly evidences the formation of needle-like acicular structures. The branching features disclose the anisotropic grain growth creating a distinctive granular structure in the NCD_{15} films. The c-DF-TEM micrographs of the films evinces in Figure $4d_2$ show evidently the formation of needle-like diamond grains with graphitic domains (green feature) surrounding the diamond grain. Figure 5d shows the HR-TEM image of the designated region "D" in NCD_{15} films (Figure $4d_1$) which displays a clear core-shell microstructure in which the needle-like diamond grains are encased by the graphite layers. The thickness of the graphite layers varies from a few atomic layers to more than 5 layers. The FT image of the entire structure image (FT_{0d}) shows that in addition to the diffraction spots, which matches up to diamond grain, there is a thick central diffuse ring which corresponds to the graphite phase, as it is of donut-shape. The presence of diamond (region "d1") and diamond and graphite (region "d2") and graphite (region "d3") is highlighted by ft-images, ft_{d1}, ft_{d2}, and ft_{d3} images, respectively.

The CC dependent microstructural changes of the NCD films reflect in the electrical properties of the film. The electrical resistivity of the films were measured using four probe technique and the values are tabulated in Table 2. With increasing CC the resistivity follows a downward trend starting from highest value of 1.5×10^8 Ω.cm of NCD_1 and finally reaches to 90 Ω.cm in case of NCD_{15}.

Table 2 Resistivity values of NCDz films.

View Article Online
DOI: 10.1039/C9TA04165F

CH_4 concentration (%)	Resistivity (Ω.cm)
1	$1.5*10^8$
5	$2.5*10^5$
10	$2*10^2$
15	$9*10^1$

With these observations, we have explained the mechanism of the wettability on the NCD films. First, based on their chemical states, the NCD films show different wettability properties. It is known that the surface energy of (100) and (111) planes of diamond are 9207 and 3387 mJ/m^2, whereas in case of highly ordered pyrolytic graphite it is 1139 mJ/m^2.[65, 66] This suggests that an sp^2 rich surface is responsible for reduction in the surface energy, hence increasing hydrophobicity in the diamond film by decreasing the surface dangling bonds.[67] Detailed spectroscopic and microscopic investigations confirm that with increasing CC, the fraction of sp^2 bonded atoms on the NCD surface is increased, in turn decreasing the surface energy with the enhancement in the hydrophobic nature of NCD films. Secondly, the morphology, porosity and roughness are also crucial for controlling the wetting behavior.[68] Conventional principles of roughness dependent wettability of Wenzel[8] and Cassie-Baxter[69] lead to the fact that the increment in the surface roughness enhances the underlying wetting nature of the substrate, i.e., hydrophilic becomes more hydrophilic and hydrophobic becomes more hydrophobic with the increase in the surface roughness. The smooth polycrystalline diamond thin film was hydrophilic in nature (around 64°)[11] but all the NCD films have demonstrated in this work show hydrophobic behavior, which is supported by the chemical nature of localized functional groups associated with the micro/nano features of NCD. The change in the wettability due to the increasing CC can be explained with the Wenzel and Cassie-Baxter model, and a complete or incomplete transition from a Cassie-Baxter to Wenzel state has been systematically achieved by submitting the NCD to electrowetting. The AFM result indicates that surface roughness increases with the CC (see Figure 2f) and a maximum roughness was achieved for NCD_{15}. This enhancement in the roughness enhances the trapped air inside the micro/nano cavities that leads to Cassie-Baxter state. Naha et al.[70] suggested that spherical grains are preferable for hydrophobicity. In the case of 5% CC (NCD_5) and onwards a clear spherical grains are evident whereas the NCD_{15} resulted in a needle-like structure which is even more favourable for a Cassie-Baxter state. Between the NCD_5 and NCD_{10} films, a very minimal change in spherical morphologies was noticed, as can be seen in Figure 2c and d. Therefore, entrapped air can no longer make a huge difference in the CA response of NCD_5 and NCD_{10} sample, irrespective of the other effects like surface bonding states, surface passivation etc. come into play, which seems to have less influence compared to the air capillarity. Yan *et al.*[71] also found this type of effect in CA measurements using spherical surfaces. Therefore, the combined effect of a high percentage of sp^2 hybridized carbon, high aspect ratio of nanoneedles, and high roughness are a prerequisite for high WCA (θ_{NCD15} ~ 142°) of the NCD_{15} sample.

With the help of electrowetting, the very systematic transition from metastable (Cassie-Baxter) to stable state (Wenzle) is obtained. The role of the external applied field, presence of ions in electrolytes, formation of electric double layer, the role of water

DOI: 10.1039/C9TA04165F

electrolysis, and the microstructural properties of NCD films are equally responsible for this irreversible change in the wettability of the NCD films.[48] During the actuation (+ve bias applied to NCD films), i.e., electrolysis, the hydrogen ion (H^+) gets attracted towards the Cu electrode whereas, the hydroxyl ions (OH^-) gather at the liquid-solid (NCD) interface. We believe that the ions from the KCl electrolyte facilitates this process. Because NCD_5 sample has more oxygen containing functional groups attached to the sp^2 sites as compared to NCD_1 (see Figure S3 in supporting information), which favours the electrochemical oxidation of NCD hybrid acting as an anode.[48] Therefore, oxidized NCD_5 film is responsible for the drastic non-linear transition from a non-wettable to wettable state (CB-Wn). Especially the unstable n-D phase of NCD_5 (cf Figure. $4b_1$ and 5b) is facilitating the electrochemical oxidation on the NCD_5 surface, which results in a permanent transition from CB-Wn state. No such complications arise when NCD_5 is acting as a cathode because of the electrostatic repulsion of OH^- ions. Therefore, asymmetric electrowetting is a direct consequence of electrochemical oxidation caused by the attached oxygen groups at the NCD_5 surface. With further increasing applied potential, either the hydrogen ion absorption saturates or all the air pockets have been filled by liquid.[18,36] This in turn results in a constant CA after a certain voltage. Interestingly, NCD_{15} shows the symmetric variation of contact angle in both +ve and –ve applied bias even though the sample has a significant amount of oxygen containing groups (Figure S3, supporting information). This can be explained on the basis of electrostatic pressure generated at the three phase contact line due to the presence of excess amount charge carriers which is independent of polarity of the voltage applied.[76] It is known that the CA response to an external voltage is described by the Young-Lippmann equation.[15]

$$Cos\theta = Cos\theta o + \frac{CV^2}{2\Upsilon_{LV}} \quad (1)$$

where, θo is the initial CA or Young's CA of a liquid with interfacial tension, Υ_{LV}; θ is the apparent CA observed due to the application of external voltage and C is the interfacial capacitance. Therefore, the interfacial capacitance is also an influencing factor under consideration, while performing the electrospreading on NCD films. After careful observation of Eq(1), it is clear that for a constant interfacial tension, the apparent contact angle is directly proportional to the CV^2. Thus, for the same applied voltage the capacitance is the only decisive factor that will dictate the electrospreading. From Figure 1b it is worthwhile to note that for NCD_1 and NCD_3 this capacitance effect is linear and independent of polarity. Interestingly the nonlinear behavior in equivalent capacitance was observed for NCD_5, NCD_{10} and NCD_{15}. Moreover, the saturation in the contact angle leads us to believe that the capacitance might also reach its peak. The linear behavior of capacitance in NCD_1 and NCD_3 can be explained by considering the fact that the diamond layer is acting as an dielectric layer on top Si(100) substrate and following the conventional electrowetting on dielectric model where relatively low interfacial capacitance is responsible for slower CA response with applied dc bias.[77,78] Whereas, much faster CA change in the NCD_5, NCD_{10} and NCD_{15} due to the high percentage of surface oxygen functionalities are responsible for non-linear variation in capacitance.[79]Though, other factors such as the degree of penetration, surface diffusion, electrolyte pH, etc. could also contribute to such electrowetting properties of these hybrid NCD films and in order to understand the mechanism more clearly, further characterization is required.

Conclusions

A combination of sp^2 and sp^3 carbon hybrids with high hydrophobicity and fascinating electrowetting properties have been prepared successfully. These properties can be readily controlled by manipulating the fraction of sp^2 bonded carbon in the hybrid films and by regulating the morphology and microstructure at the nanoscale. We put forward that the induced roughness in the diamond nanostructures and increasing fraction of sp^2 bonded carbon with increasing CH_4 concentration contribute to the enhanced hydrophobicity and attractive electrowetting behavior of NCD surfaces, which is explained on the basis of the Cassie Baxter-to-Wenzel transition model. The strong polarity dependent electrowetting, especially for NCD_5 and NCD_{10} samples, is explained by the attachment of oxygen containing functional groups at the film surface, which is responsible for a rapid transition from non-wetting to wetting state. Therefore the optimization of film composition is considered to be the key factor to attain these desirable surface properties. When the CC is maximum, i.e. NCD_{15} films with needle-like geometry where diamond grains are surrounded by graphitic phases, are the most auspicious one for producing nearly superhydrophobic surface. On the other hand water can efficiently wet the NCD_5 films with granular geometry, just by applying a small 5 V dc bias. Hence, in a time of high demand for new carbon based material in the area of energy storage, microfluidics, and faster electronic devices, the present work is a facile way for production of hybrid carbon nanostructure consists of sp^2 carbon coupled with diamond. The precise and fast control over the wettability by means of electrowetting with NCD nanostructures will be a promising alternative to numerous applications.

Conflicts of interest

There are no conflicts to declare.

Acknowledgements

D. Banerjee is indebted to Shiv Nadar University for providing Ph.D. scholarship. Dr. K. J. Sankaran and Dr. K. Haenen like to thank the financial support of the Methusalem "NANO" network. S. Deshmukh and Dr. P. R. Waghmare like to thank Natural Science and Engineering Research Council (NSERC) for the financial support in the form of Grant No. RGPIN-2015-06542. The authors would like to thank Mr. Juan Sebastian Marin Quintero for helping in electrowetting experiments.

References

1. X. Yao, Y. Song and L. Jiang, *Adv. Mater.*, 2011, **23**, 719-734.
2. X. Zhang, F. Shi, J. Niu, Y. Jiang and Z. Wang, *J. Mater. Chem.*, 2008, **18**, 621-633.
3. M. W. J. Prins, W. J. J. Welters and J. W. Weekamp, *Science*, 2001, **291**, 277-280.
4. M. Yoshida and J. Lahann, *ACS Nano*, 2008, **2**, 1101-1107.
5. A. Zeira, D. Chowdhury, R. Maoz and J. Sagiv, *ACS Nano*, 2008, **2**, 2554-2568.
6. W. Song, D. D. Veiga, C. A. Custódio and J. F. Mano, *Adv. Mater.*, 2009, **21**, 1830-1834.
7. L. Feng, S. Li, Y. Li, H. Li, L. Zhang, J. Zhai, Y. Song, B. Liu, L. Jiang and D. Zhu, *Adv. Mater.*, 2002, **14**, 1857-1860.

8. R. N. Wenzel, *Ind. & Eng. Chem.*, 1936, **28**, 988-994.
9. J. Yuan, X. Liu, O. Akbulut, J. Hu, S. L. Suib, J. Kong and F. Stellacci, *Nat. Nanotechnol.*, 2008, **3**, 332.
10. X. Yang, J. Zhuang, X. Li, D. Chen, G. Ouyang, Z. Mao, Y. Han, Z. He, C. Liang, M. Wu and J. C. Yu, *ACS Nano*, 2009, **3**, 1212-1218.
11. S. Tian, W. Sun, Z. Hu, B. Quan, X. Xia, Y. Li, D. Han, J. Li and C. Gu, *Langmuir*, 2014, **30**, 12647-12653.
12. A. G. Montaño-Figueroa, J. J. Alcantar-Peña, P. Tirado, A. Abraham, E. de Obaldia and O. Auciello, *Carbon*, 2018, **139**, 361-368.
13. Q. Wang, J. Bai, B. Dai, L. Yang, P. Wang, Z. Yang, S. Guo, Y. Zhang, J. Han and J. Zhu, *Carbon*, 2018, **129**, 367-373.
14. L.-P. Xu, D. Han, X. Wu, Q. Zhang, X. Zhang and S. Wang, *Sci. Rep.*, 2016, **6**, 38016.
15. F. Mugele and J.-C. Baret, *J. phys. condens. matter*, 2005, **17**, R705.
16. B. A. Kakade, *Nanoscale*, 2013, **5**, 7011-7016.
17. T. M. Babinec, B. J. Hausmann, M. Khan, Y. Zhang, J. R. Maze, P. R. Hemmer and M. Lončar, *Nat. nanotechnol.*, 2010, **5**, 195.
18. J. Pu, S. Wan, Z. Lu, G.-a. Zhang, L. Wang, X. Zhang and Q. Xue, *J. Mat. Chem. A*, 2013, **1**, 1254-1260.
19. T. H. Bointon, M. D. Barnes, S. Russo and M. F. Craciun, *Adv. Mater.*, 2015, **27**, 4200-4206.
20. Y. Zhai, Y. Dou, D. Zhao, P. F. Fulvio, R. T. Mayes and S. Dai, *Adv. mater.*, 2011, **23**, 4828-4850.
21. F. Gao and C. E. Nebel, *ACS Appl. Mater. Interfaces*, 2016, **8**, 28244-28254.
22. K. Siuzdak, M. Ficek, M. Sobaszek, J. Ryl, M. Gnyba, P. Niedziałkowski, N. Malinowska, J. Karczewski and R. Bogdanowicz, *ACS Appl. Mater. Interfaces*, 2017, **9**, 12982-12992.
23. S. Deshmukh, K. J. Sankaran, S. Korneychuk, J. Verbeeck, J. McLaughlin, K. Haenen and S. S. Roy, *Electrochim. Acta*, 2018, **283**, 1871-1878.
24. W. Zhu, G. P. Kochanski and S. Jin, *Science*, 1998, **282**, 1471-1473.
25. S. D. Janssens, S. Drijkoningen, M. Saitner, H.-G. Boyen, P. Wagner, K. Larsson and K. Haenen, *J. Chem. Phys.*, 2012, **137**, 044702.
26. H. Zhuang, B. Song, V. V. S. S. Srikanth, X. Jiang and H. Schönherr, *J. Phys. Chem. C*, 2010, **114**, 20207-20212.
27. W. Yang, O. Auciello, J. E. Butler, W. Cai, J. A. Carlisle, J. E. Gerbi, D. M. Gruen, T. Knickerbocker, T. L. Lasseter, J. N. Russell Jr, L. M. Smith and R. J. Hamers, *Nat. Mater.*, 2002, **1**, 253.
28. Y. Coffinier, S. Szunerits, H. Drobecq, O. Melnyk and R. Boukherroub, *Nanoscale*, 2012, **4**, 231-238.
29. Y. Kaibara, K. Sugata, M. Tachiki, H. Umezawa and H. Kawarada, *Diam. Relat. Mater.*, 2003, **12**, 560-564.
30. J. W. Yi, M.-W. Moon, S. F. Ahmed, H. Kim, T.-G. Cha, H.-Y. Kim, S.-S. Kim and K.-R. Lee, *Langmuir*, 2010, **26**, 17203-17209.
31. S. C. H. Kwok, J. Wang and P. K. Chu, *Diam. Relat. Mater.*, 2005, **14**, 78-85.
32. K. Panda, N. Kumar, B. K. Panigrahi, S. R. Polaki, B. Sundaravel, S. Dash, A. K. Tyagi and I. N. Lin, *Tribol. Int.*, 2013, **57**, 124-136.
33. J. H. C. Yang and K. Teii, *Diam. Relat. Mater.*, 2012, **24**, 54-58.
34. M. Karlsson, P. Forsberg and F. Nikolajeff, *Langmuir*, 2010, **26**, 889-893. View Article Online DOI: 10.1039/C9TA04165F
35. W. J. Zhang, X. M. Meng, C. Y. Chan, Y. Wu, I. Bello and S. T. Lee, *Appl. Phys. Lett.*, 2003, **82**, 2622-2624.
36. B. Kakade, R. Mehta, A. Durge, S. Kulkarni and V. Pillai, *Nano Lett.*, 2008, **8**, 2693-2696.
37. J. Robertson, *Prog. Solid State Chem.*, 1991, **21**, 199-333.
38. J. Robertson, *Journal*, 1994, **66**, 1789.
39. P. J. King, U. Khan, M. Lotya, S. De and J. N. Coleman, *ACS Nano*, 2010, **4**, 4238-4246.
40. T.-K. Hong, D. W. Lee, H. J. Choi, H. S. Shin and B.-S. Kim, *ACS Nano*, 2010, **4**, 3861-3868.
41. P. K. Sow, S. Prass and W. Mérida, *ACS Appl. Mater. Interfaces*, 2015, **7**, 22029-22035.
42. E. L. Silva, Y. K. Mishra, A. J. S. Fernandes, R. F. Silva, J. Strobel, L. Kienle, R. Adelung, F. J. Oliveira and M. L. Zheludkevich, *Adv. Mater. Interfaces*, 2017, **4**, 1700019.
43. Y. Zhu, J. Zhang, Y. Zheng, Z. Huang, L. Feng and L. Jiang, *Adv. Funct. Mater.*, 2006, **16**, 568-574.
44. J. T. Han, S. Y. Kim, J. S. Woo and G.-W. Lee, *Adv. Mater.*, 2008, **20**, 3724-3727.
45. S. Sethi and A. Dhinojwala, *Langmuir*, 2009, **25**, 4311-4313.
46. L. Zhu, J. Xu, Y. Xiu, Y. Sun, D. W. Hess and C.-P. Wong, *The J. Phys. Chem. B*, 2006, **110**, 15945-15950.
47. O. A. Williams, O. Douhéret, M. Daenen, K. Haenen, E. Ōsawa and M. Takahashi, *Chem. Phys. Lett.*, 2007, **445**, 255-258.
48. Z. Wang, L. Ci, L. Chen, S. Nayak, P. M. Ajayan and N. Koratkar, *Nano Lett.*, 2007, **7**, 697-702.
49. R. Paul, S. N. Das, S. Dalui, R. N. Gayen, R. K. Roy, R. Bhar and A. K. Pal, *J. Phys. D: Appl. Phys.*, 2008, **41**, 055309.
50. M. Mertens, M. Mohr, K. Brühne, H. J. Fecht, M. Łojkowski, W. Święszkowski and W. Łojkowski, *Appl. Surf. Sci.*, 2016, **390**, 526-530.
51. O. Auciello, J. Birrell, J. A. Carlisle, J. E. Gerbi, X. Xiao, B. Peng and H. D. Espinosa, *J. Phys. Condens. Matter*, 2004, **16**, R539.
52. B. Puri and P. Walker, *Chemistry and Physics of Carbon. Marcel Dekker, New York*, 1970, 191-282.
53. E. J. Mele and J. J. Ritsko, *Phys. Rev. Lett.*, 1979, **43**, 68-71.
54. J. Robertson and E. P. O'Reilly, *Physical Review B*, 1987, **35**, 2946-2957.
55. R. E. Shroder, R. J. Nemanich and J. T. Glass, *Phys. Rev. B*, 1990, **41**, 3738-3745.
56. K. Kobashi, K. Nishimura, Y. Kawate and T. Horiuchi, *Phys. Rev. B*, 1988, **38**, 4067-4084.
57. M. Frenklach and H. Wang, *Phys. Rev. B*, 1991, **43**, 1520-1545.
58. C. Mapelli, C. Castiglioni, G. Zerbi and K. Müllen, *Phys. Rev. B*, 1999, **60**, 12710-12725.
59. J. F. Morar, F. J. Himpsel, G. Hollinger, J. L. Jordan, G. Hughes and F. R. McFeely, *Phys. Rev. B*, 1986, **33**, 1340-1345.
60. S. Osswald, G. Yushin, V. Mochalin, S. O. Kucheyev and Y. Gogotsi, *J. Am. Chem. Soc.*, 2006, **128**, 11635-11642.
61. F. L. Coffman, R. Cao, P. A. Pianetta, S. Kapoor, M. Kelly and L. J. Terminello, *Appl. Phys. Lett.*, 1996, **69**, 568-570.
62. J. Kulik, G. D. Lempert, E. Grossman, D. Marton, J. W. Rabalais and Y. Lifshitz, *Phys. Rev. B*, 1995, **52**, 15812-15822.
63. J. Xiao, J. Li, P. Liu and G. Yang, *Nanoscale*, 2014, **6**, 15098-15106.

View Article Online
DOI: 10.1039/C9TA04165F

64. H. HIRAI and K.-I. KONDO, *Science*, 1991, **253**, 772-774.
65. T. Takai, T. Halicioğlu and W. A. Tiller, *Surf. Sci.*, 1985, **164**, 341-352.
66. S. K. Rhee, *J. Am. Ceram. Soc.*, 1972, **55**, 300-303.
67. L. Sun, P. Guo, X. Li and A. Wang, *Diam. Relat. Mater.*, 2017, **73**, 278-284.
68. D. Banerjee, S. Mukherjee and K. K. Chattopadhyay, *Carbon*, 2010, **48**, 1025-1031.
69. A. Cassie and S. Baxter, *Trans. Faraday soc.*, 1944, **40**, 546-551.
70. S. Naha, S. Sen and I. K. Puri, *Carbon*, 2007, **8**, 1702-1706.
71. L. Yan, K. Wang, J. Wu and L. Ye, *Colloids Surf. A: Physicochemical and Engineering Aspects*, 2007, **296**, 123-131.
72. B.-E. Park and H. Ishiwara, *Appl. Phys. Lett.*, 2003, **82**, 1197-1199.
73. B. Li, D. Yu and S.-L. Zhang, *Phys. Rev. B*, 1999, **59**, 1645-1648.
74. S. C. Ray, H. M. Tsai, J. W. Chiou, B. Bose, J. C. Jan, K. Kumar, W. F. Pong, D. Dasgupta and M. H. Tsai, *J. Phys. Condens. Matter*, 2004, **16**, 5713-5719.
75. H. K. Jeong, H. J. Noh, J. Y. Kim, M. H. Jin, C. Y. Park and Y. H. Lee, *EPL*, 2008, **82**, 67004.
76. K. H. Kang, *Langmuir*, 2002, **18**, 10318-10322.
77. V. Narasimhan and S.-Y. Park, *Langmuir*, 2015, **31**, 8512-8518.
78. M. J. Schertzer, R. Ben-Mrad and P. E. Sullivan, *Sens. Actuators B-Chem.*, 2010, **145**, 340-347.
79. A. G. Pandolfo and A. F. Hollenkamp, *J. Power Sources*, 2006, **157**, 11-27.

View Article Online
DOI: 10.1039/C9TA04165F

Direct Synthesis of Electrowettable Nanostructured Hybrid Diamond

Sujit Deshmukh[a,b], Kamatchi Jothiramalingam Sankaran[c,d], Debosmita Banerjee[a], Chien-Jui Yeh[e], Key-Chyang Leou[e], Deodatta Maheshwar Phase[f], Mukul Gupta[f], I-Nan Lin[g], Ken Haenen[c,d], Susanta Sinha Roy[a*], Prashant. R. Waghmare[b*]

[a]Department of Physics, School of Natural Sciences, Shiv Nadar University, NH-91, Uttar Pradesh 201314, India.

[b] *interfacial* Science and Surface Engineering Lab (*i*SSELab), Department of Mechanical Engineering, University of Alberta, Edmonton, Alberta T6G2G8, Canada

[c]Institute for Materials Research (IMO), Hasselt University, Diepenbeek, Belgium.

[d]IMOMEC, IMEC vzw, Diepenbeek, Belgium.

[e]Department of Engineering and System Science, National Tsing Hua University, Hsinchu, Taiwan, Republic of China.

[f]UGC-DAE Consortium for Scientific Research, University Campus, Khandwa Road, Indore 452017, India.

[g]Department of Physics, Tamkang University, Tamsui, Taiwan, Republic of China.

*Corresponding authors

Email addresses: susantaroy69@gmail.com and waghmare@ualberta.ca

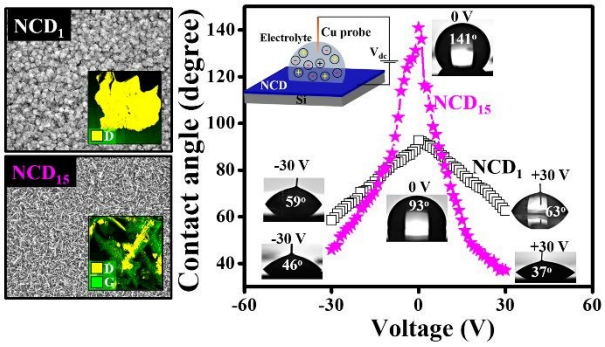

Low voltage wetting transition from Cassie-Baxter to Wenzel state is achieved by preparing needle like conductive diamond-graphite core shell nanostructure.